Surface & Coatings Technology 411 (2021) 126915

Contents lists available at ScienceDirect

Surface & Coatings Technology

journal homepage: www.elsevier.com/locate/surfcoat

Oxidation-resistant coating of FeCrAl on Zr-alloy tubes using 3D printing direct energy deposition

Il-Hyun Kim [a,b], Yang-Il Jung [a,*], Hyun-Gil Kim [a], Jae-Il Jang [b]

[a] Advanced 3D Printing Technology Division, Korea Atomic Energy Research Institute, Daejeon 34057, Republic of Korea
[b] Division of Materials Science and Engineering, Hanyang University, Seoul 04765, Republic of Korea

ARTICLE INFO

Keywords:
3D printing
FeCrAl
Zr alloy
Direct energy deposition
Oxidation resistance

ABSTRACT

Zr-alloys are used as nuclear fuel cladding tubes in nuclear reactors. Recently, surface coating of conventional Zr-alloy tubes has been performed to enhance their resistance to corrosion and high-temperature oxidation. FeCrAl is a candidate coating material because of its extremely low oxidation rates and desirable mechanical properties. In this study, FeCrAl was deposited directly on a Zr-alloy using 3D printing technology. The processing conditions, such as laser beam power, scanning speed, and powder/gas feed rates, were optimized to attain a dense and adhesive FeCrAl layer. The minimum beam power required to melt the FeCrAl source powder was found to be 160 W. The FeCrAl layer coagulated when the scanning speed was low and the powder feed rate was high, and it became sparse and porous when the scanning speed was high and feed rate was low. The FeCrAl-coated Zr samples were tested for oxidation at 1200 °C. A thin Al_2O_3 (2–3 μm) formed on the FeCrAl surface, and a diffusion layer developed between the FeCrAl/Zr interfaces. By comparison, a thick ZrO_2 (approximately 120 μm) layer formed in the Zr-alloy without coating. The oxidation resistance of the Zr-alloys increased by approximately 50 times by the formation of FeCrAl layer on their surfaces. This 3D printing method is expected to improve the safety of Zr fuel cladding tubes.

1. Introduction

Zr-alloys have been used as fuel cladding tubes in nuclear power plants owing to their excellent corrosion resistance, mechanical properties, and neutron economy during normal operating conditions. However, their durability is affected by rapid oxidation and exothermic reactions when exposed in air/steam at high-temperature (>900 °C) [1,2]. Thus, accident-tolerant fuel claddings are being developed globally with a demand for nuclear fuels with higher safety under normal operation and severe accident conditions. Accident-tolerant fuel cladding has greater resistance to high-temperature oxidation and deformation than conventional cladding; it reduces oxidation-induced hydrogen generation, suppressing the risk of hydrogen explosion and exposure of radioactive materials due to deformation failure. Studies on accident-tolerant fuel cladding include the development of coating technologies applicable to current Zr claddings [3–8], and alternative materials to replace Zr-alloys [9–11]. In particular, coating technology has attracted much interest as an accident-tolerant fuel cladding manufacturing technology because it can improve corrosion and oxidation resistance without changing the Zr base material, which makes it easier than developing a new material.

The materials considered for coating include Cr [3–7], CrAl [4], and FeCrAl [6,8]. Among them, FeCrAl alloy is also considered a promising material for replacing Zr cladding [9]. We have sought to improve the insufficient high-temperature oxidation resistance of Zr cladding by coating it with a FeCrAl material [6]. Previously, FeCrAl was coated using a cold spray method. The cold spray method is a fast coating method at low temperature using compressed gas; however, it has disadvantages such as plastic deformation that increases the strength of the coating layer [12], poor adhesive property of the coating layer and the base material [13], and the mismatch between the coating layer and the theoretical density [14]. In the present study, FeCrAl coating was conducted using a 3D laser printing method to resolve these problems.

The 3D laser printing method is largely divided into the powder bed fusion (PBF) method and the direct energy deposition (DED) method. The PBF method forms a laminated structure within a powder bed on the stage using a laser heat source, and the DED method laminates and coats the powder using the powder feeder through the nozzle directly with the laser heat source. The PBF method utilizes a powder bed containing uniform spherical particles; therefore, it is possible to fabricate bulky

* Corresponding author.
E-mail address: yijung@kaeri.re.kr (Y.-I. Jung).

https://doi.org/10.1016/j.surfcoat.2021.126915
Received 24 November 2020; Received in revised form 6 January 2021; Accepted 14 January 2021
Available online 3 February 2021

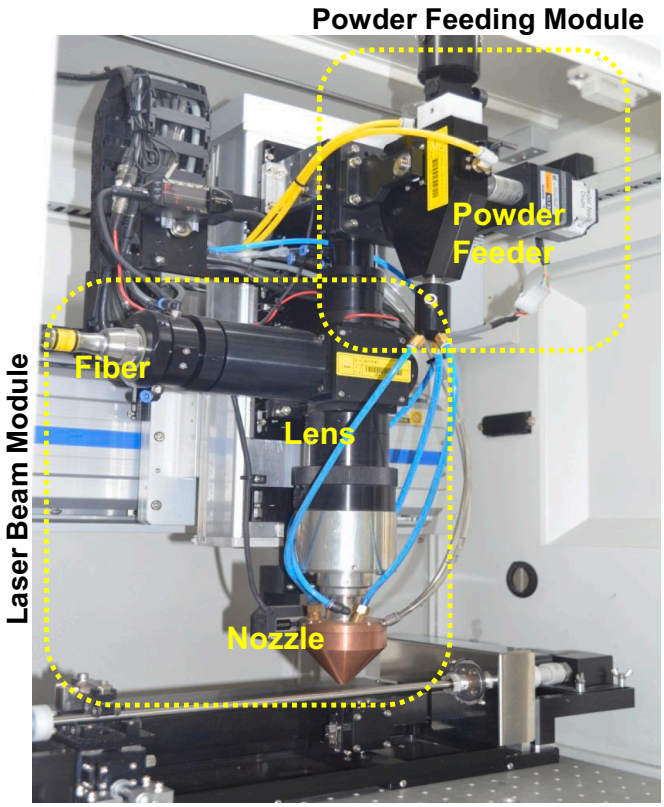

Fig. 1. Laser equipment for 3D printing consisting of a laser beam module and powder feeding module.

and complex structural parts, but it is impossible to coat them on tubes. The DED method is not restricted to the powder shape, and the laser heat source is directly applied, which allows for coating on plates and tubes regardless of the shape. It also ensures that the lamination and coating are as close to the theoretical density as possible. Therefore, the FeCrAl coating was performed using the DED method in this study. The processing conditions, such as laser beam power, scanning speed, and powder/gas feed rates, were optimized to attain a uniform FeCrAl coating layer. The microstructural characteristics, adhesion properties, and oxidation behavior of the FeCrAl-coated Zr-alloy samples were evaluated.

2. Experimental procedures

2.1. 3D printing laser equipment

Fig. 1 shows a photograph of the 3D laser printer equipment utilized in this study, which consists of a laser beam module (nozzle, lens assembly, optical fibers, and laser source) and a powder feeding module. The laser source (PF-1500F, HBL Co., Korea) used a continuous wave diode laser with a maximum output of 250 W. The quality of the laser (size, density and shape) was controlled by lens assembly. It was applied the circular beam with diameter of 240 μm (D = 0.24 mm) in this experiment. When using 3D laser coating, the important parts of the equipment are the nozzle and powder feeder, because the coating uniformity and adhesion property can be varied based on the combination of the two parts [5]. The nozzle allows for positioning powders at the center of the laser beam, and the powder feeder provides a consistent amount of powder. In addition, a tubular sample is mounted on the stage, and it is designed so that cooling water can be supplied into the tube to suppress the microstructural change and deformation caused by the laser beam heat source. To prevent surface oxidation of the cladding during coating, Ar gas was supplied through the nozzle.

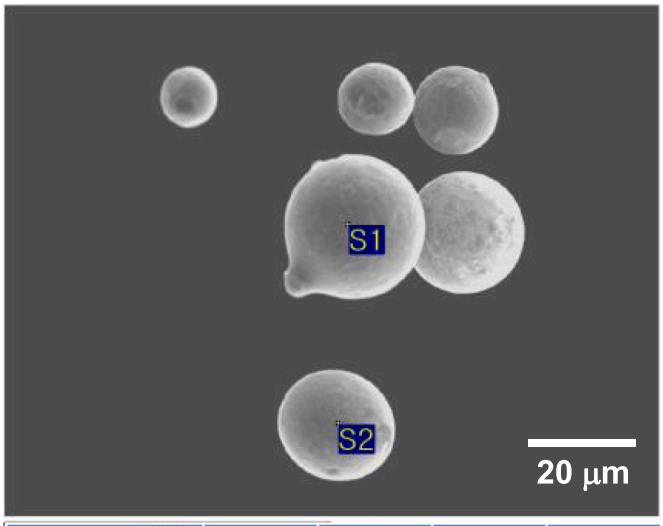

Composition	Fe	Cr	Al	Mo
S1 (wt.%)	68.65	23.06	4.97	3.32
S2 (wt.%)	68.39	22.49	5.65	3.47

Fig. 2. Appearance and chemical compositions of as-received FeCrAl particles used for the 3D printing.

2.2. Materials and processes

Commercially available Zr-alloy (Zircaloy-4, Zr-1.5Sn-0.2Fe-0.1Cr, wt%) tubes with an outer diameter of 9.5 mm and a wall thickness of 0.57 mm were used as substrate tubes. The initial microstructure of the tube was stress-relieved. Prior to coating, the tubes (400 mm in length) were cleaned with ethanol and acetone to remove debris or stains and then dried in a vacuum oven. FeCrAl powder (APMT, Sandvik AB, Sweden) with a composition of Fe-22Cr-5Al-3Mo (wt%) and purity of 99.9% was used as the coating raw material. The particle size of the powder was 20–40 μm. Fig. 2 shows a scanning electron microscopy (SEM) image of the powders used in the experiment. The shape of the powder was spherical and the measured composition was consistent with the APMT composition.

The 3D laser coating processing conditions were 140–220 W of the applied laser beam power, 5–10 mm/s range of scan speed, 0.7–2.5 g/min range of powder supply, and a flow gas (Ar) amount variable of 3.0–3.6 L/min. The rough surface was polished after 3D printing. The polished samples were subjected to high-temperature oxidation tests using a thermo-gravimetric instrument. For the high-temperature oxidation test, Zr-alloy tubes with and without FeCrAl coating were cut along the axial direction to a length of 10 mm. The samples were cleaned with ethanol under ultrasonication for 5 min and dried. Then, the samples were mounted in the test instrument. The temperature of the sample was increased up to 1200 °C at a heating rate of 50 °C/min while flowing Ar gas in order to prevent oxidation during the heating lamp. Then, a mixed gas of steam and Ar was supplied at a flow rate of 10 mL/min at 1200 °C for 2000 s. After the oxidation test, the microstructures of the samples were observed using an optical microscope and a scanning electron microscope.

3. Results and discussion

3.1. 3D printing of FeCrAl on Zr-alloy

Fig. 3 shows images of the 3D laser printing process parameters and selected samples after FeCrAl coating under various laser processing conditions. For the FeCrAl coating, 3D printing parameters, such as laser

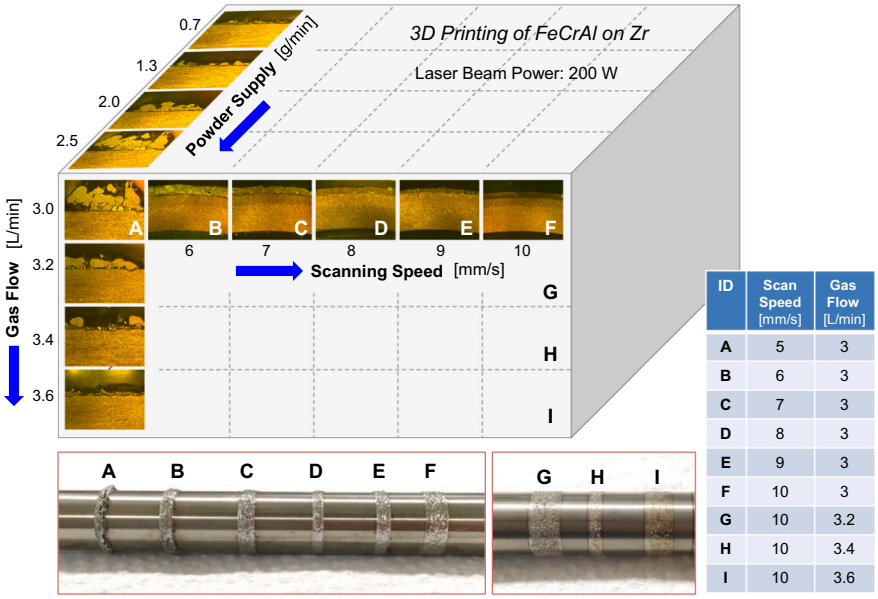

ID	Scan Speed [mm/s]	Gas Flow [L/min]
A	5	3
B	6	3
C	7	3
D	8	3
E	9	3
F	10	3
G	10	3.2
H	10	3.4
I	10	3.6

Fig. 3. Map of controlling parameters for 3D printing process and selected samples showing various morphologies of FeCrAl coatings depending on laser processing conditions.

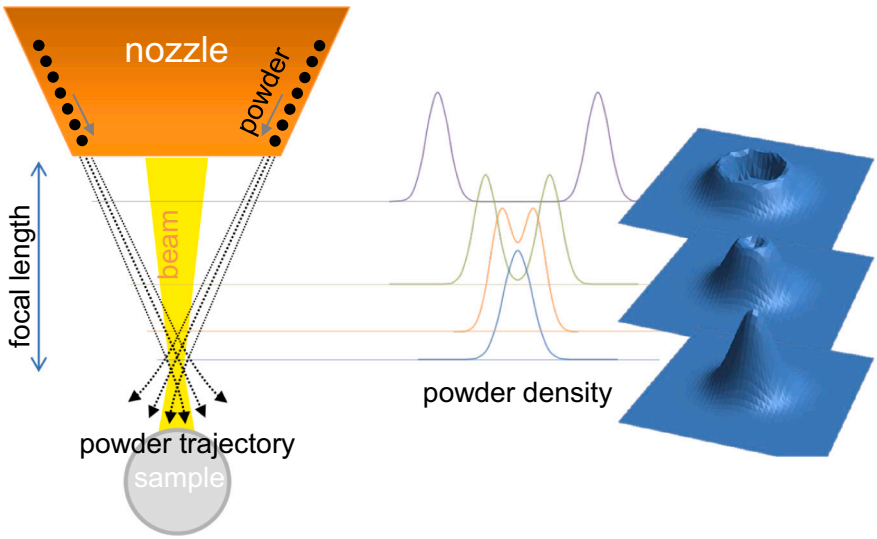

Fig. 4. Distribution of powders supplied from the nozzle head to a sample surface.

beam power, scanning speed, and powder/gas feed rates, were investigated. The applied laser beam power was varied in the range of 140–220 W. It was found the minimum required power level was 160 W. It is suggested that the threshold value for the melting of FeCrAl particles is 160 W. The scanning speed was varied in the range of 5–10 mm/s. As the scanning speed increased from 5 mm/s (A) to 10 mm/s (F), the coating thickness decreased and the surface roughness appeared to improve. The powder feed rate and flow gas were varied in the range of 0.7–2.5 g/min and 3.0–3.6 L/min, respectively. The effects of the powder feed rate and the flow gas amount were strongly correlated. As the powder feed rate increased, the coating thickness increased, but agglomerates appeared. Meanwhile, the coating thickness decreased and became sparse as the flow gas amount increased. The abundant flow gas was not desirable, as shown in Fig. 3(F–I). As the flow gas was increased from 3 L/min (F) to 3.6 L/min (I), only a small amount of powder was stuck on the surface of the Zr tube. It is considered that increasing the amount of gas led to a decrease in the amount of melted powder as the powder was spread out rather than gathered in the middle. An appropriate flow gas was required for a given powder feed rate in order to obtain a uniform coating by dispersing the supplied powder.

Fig. 4 illustrates the schematic trajectory of the powder supply during 3D printing. Powders are supplied through the rim of the nozzle head and concentrated at the focal position of the beam to obtain the maximum efficiency of powder consumption. Samples for 3D printing are usually located at the focal position. In Fig. 4, the areal density of the powders is also presented by assuming their normal distribution with respect to the height between the nozzle head and focal point. As the distance from the nozzle increases, the ridge of the powder density becomes close. At the depth of the focal point, the distribution of powders can be interpreted as a two-dimensional normal distribution:

$$g(x,y) = \frac{1}{2\pi\sigma^2} e^{-\frac{x^2+y^2}{2\sigma^2}} \quad (1)$$

where σ is the standard deviation of the distribution. The amount of powders within the beam area can be obtained by integrating Eq. (1),

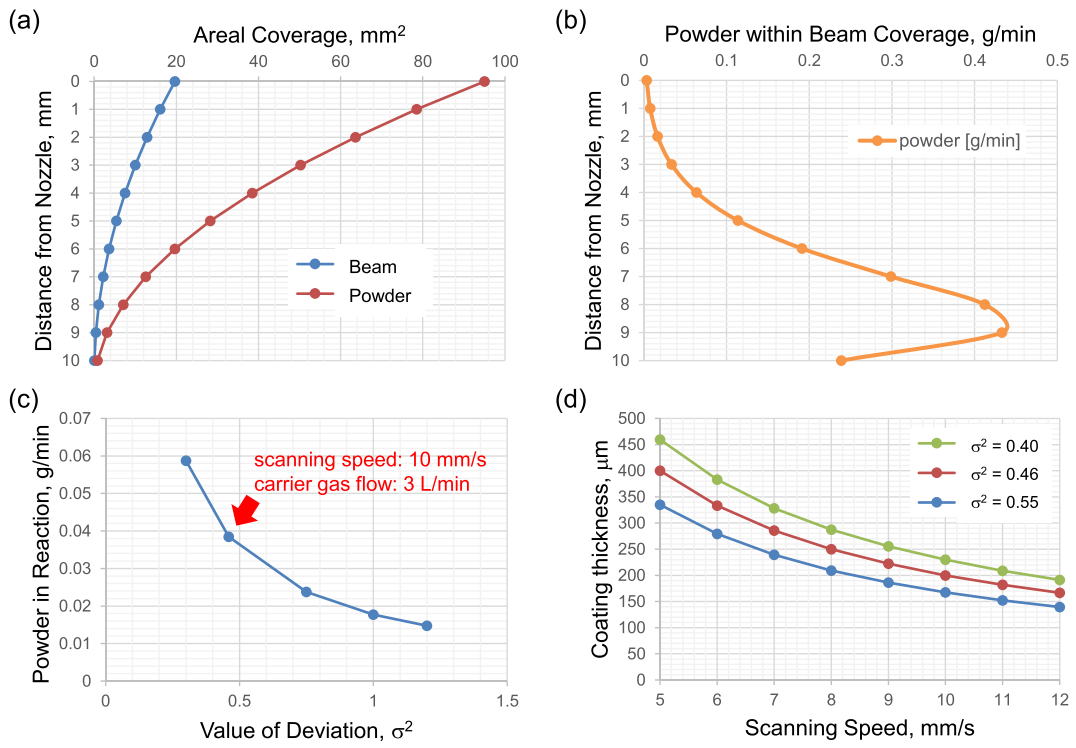

Fig. 5. Measured and estimated processing parameters for 3D printing DED: (a) areal coverage of beam and powder with respect to the distance from the nozzle head, (b) amount of powder within beam coverage with respect to the distance from the nozzle head, (c) amount of powder in reaction on sample surface, and (d) coating thickness depending on the scanning speed and standard deviation of the powder distribution.

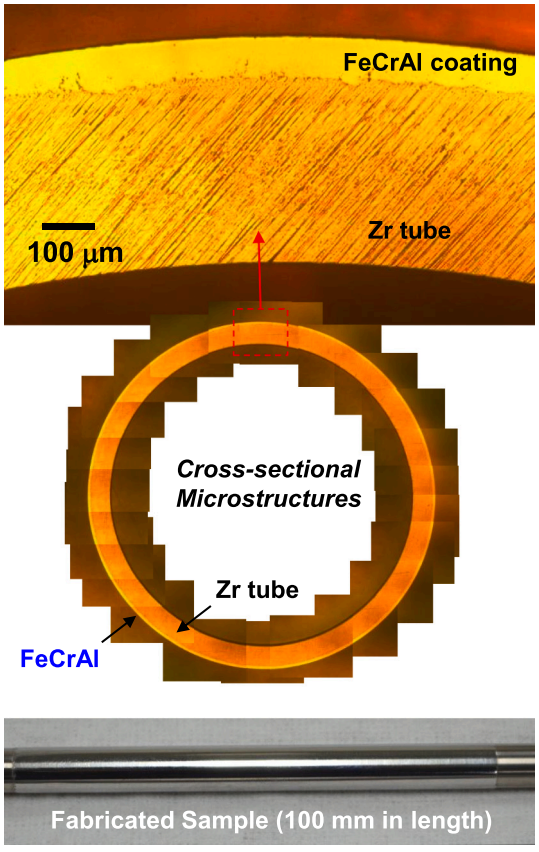

Fig. 6. Cross-sectional microstructures of FeCrAl coating layer formed on a Zircaloy-4 tube using laser 3D printing technology.

bounded by the beam radius ($D/2$).

$$w = \iint \frac{1}{2\pi\sigma^2} e^{-\frac{x^2+y^2}{2\sigma^2}} dxdy = \int_0^{D/2} \frac{1}{2\pi\sigma^2} e^{-\frac{r^2}{2\sigma^2}} drd\theta \quad (2)$$

Fig. 5(a) shows the area of the beam and powder coverage depending on the distance from the nozzle head. Because of the convergence of the beam and powder trajectory, the areal coverages decrease with distance. Fig. 5(b) shows the amount of powder within the beam area calculated numerically using Eq. (2). When the distance from the nozzle is small, the amount of powder is small because most of the powder is outside of the beam area. The amount increases with distance as the powder concentrates to the focal point. However, the amount decreases when the distance from the nozzle approaches the focal length. This is because the beam diameter is very small ($D = 0.24$ mm) compared to the powder coverage.

By varying the standard deviation of the powder density distribution, the experimental conditions were deduced, as shown in Fig. 5(c). From the experimental results, the spot of the coating had a cylindrical shape with a diameter of 0.24 mm ($D = 0.24$ mm) and height of about 200 μm when the carrier gas flow was 3.0 L/min. The mass of the spot was 6.47 $\times 10^{-5}$ g when applying a density of 7.15 g/cm^3. If the scanning speed was 10 mm/s, the rate of mass for the FeCrAl coating would be 0.0388 g/min. According to Fig. 5(c), this processing condition matches the case when $\sigma^2 = 0.46$. This condition indicates that approximately 40% of the powder is concentrated within a diameter of 1.35 mm ($\pm\sigma$) and 86% within 2.71 mm ($\pm 2\sigma$) [15]. In Fig. 5(d), the coating thickness was estimated depending on the scanning speed and standard deviation of the powder density. As the scanning speed increased, the thickness of single-layer coating decreased. The standard deviation is correlated with the carrier gas flow: a larger value (σ^2 of 0.55) indicates the broadening of powder coverage and results in decreased coating thickness, and a smaller value (σ^2 of 0.40) indicates the concentration of powder coverage and results in increased coating thickness.

Fig. 6 shows the FeCrAl-coated Zr tube sample and its cross-sectional

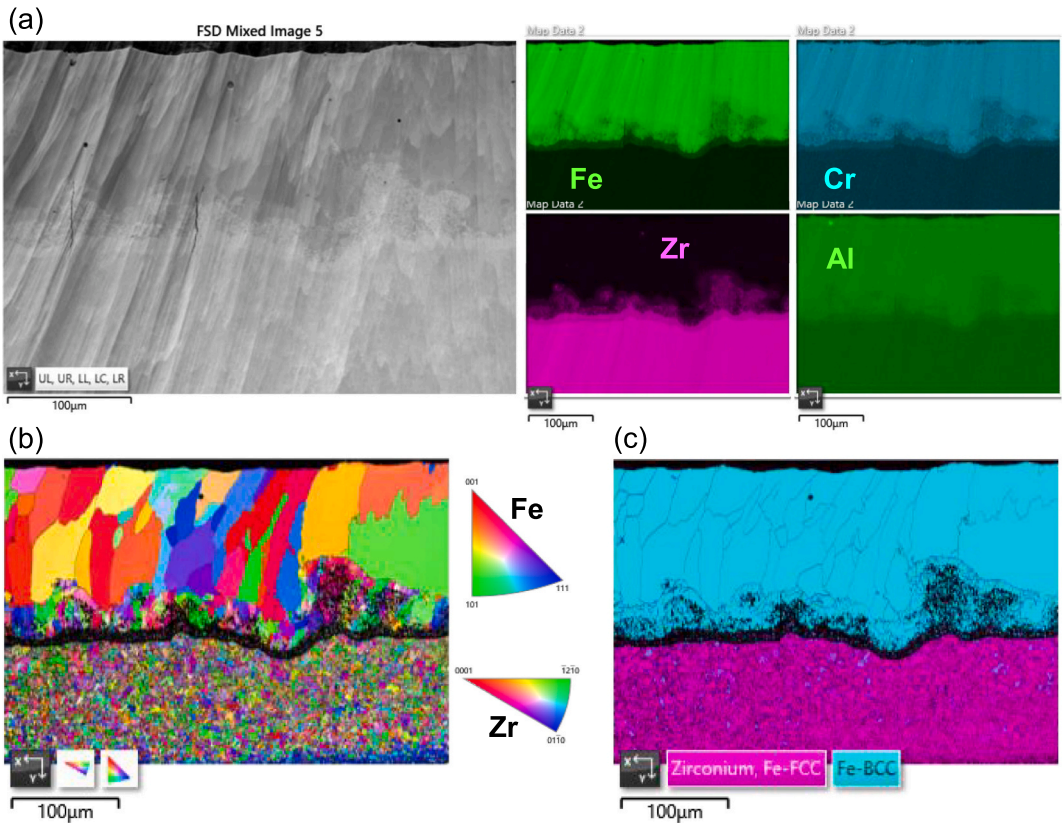

Fig. 7. (a) Interfacial microstructure and elemental profiles (Fe, Cr, Al, and Zr) for the coated FeCrAl layer on a Zr tube, and analysis results of (b) EBSD mapping and (c) crystallographic mapping of the sample.

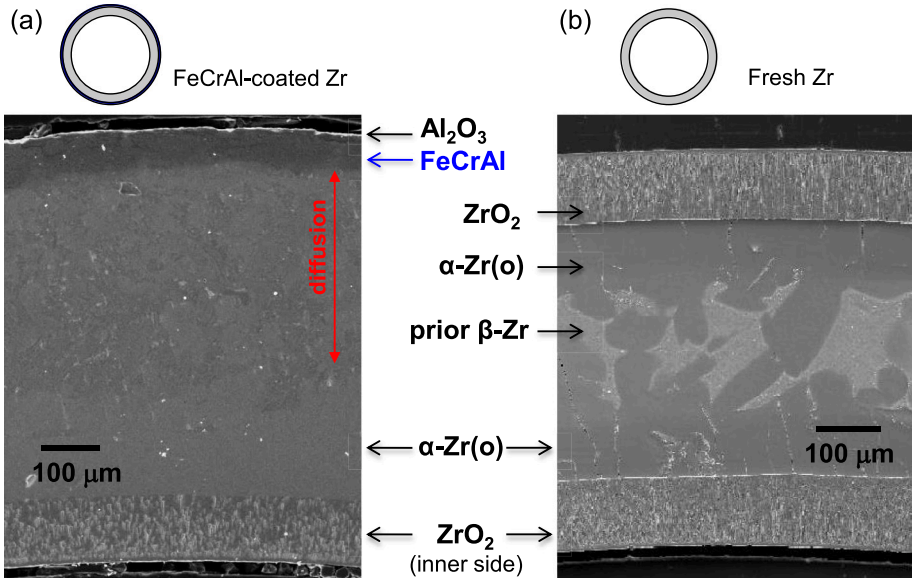

Fig. 8. Cross-sectional microstructures of (a) FeCrAl-coated Zr and (b) fresh Zr samples after a high-temperature oxidation test at 1200 °C for 2000 s in a steam environment.

microstructure. The sample was fabricated using the F condition shown in Fig. 3, i.e., 200 W power, 10 mm/s scanning speed, 2.5 g/min powder feeding, and 3.0 L/min flow gas. The specific energy for this DED process was $P/vD = 83.3$ J/mm^2 or $P/w = 309.2$ J/mg, and interaction time was $D/v = 0.024$ s. The surfaces of the 3D printing samples were rough; thus, they were polished for further microstructural and oxidation examinations. The final thickness of the coated FeCrAl layer was approximately 90 μm. The dense coating layer indicated well-established 3D printing conditions. The morphology of the FeCrAl/Zr interface was rough and irregular due to interfacial mixing of the materials. It is suggested that the FeCrAl coating layer has a high adhesion strength. In addition, the shape of the coated tube was circular and straight, as shown in Fig. 6. Because the laser heat can easily deform thin-walled tubes, it is essential to cool the tube during the 3D printing process. Therefore, the cooling

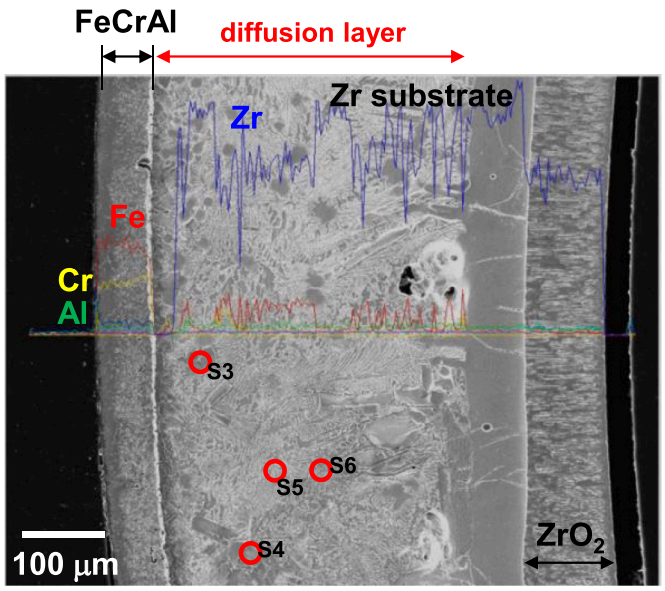

Composition	Fe	Cr	Al	Zr
S3 (wt.%)	5.46	2.06	0.58	88.75
S4 (wt.%)	27.35	19.92	1.26	50.38
S5 (wt.%)	11.48	4.99	0.65	77.95
S6 (wt.%)	17.22	0.30	0.52	78.03

Fig. 9. Elemental analyses across FeCrAl-coated Zr samples showing the diffusion layer and oxide layer that formed after the high-temperature oxidation test.

water effectively reduced the temperature rise of the tubes during the fabrication process.

The compositional change of FeCrAl was investigated before and after 3D printing. The average elemental composition of the FeCrAl coating was 66 wt% Fe, 23 wt% Cr, 7 wt% Al, and 4 wt% Mo. This composition is consistent with those of APMT and the original powder. According to the X-ray diffraction patterns for the FeCrAl source powder and FeCrAl coating layer, the phases of FeCrAl did not change during the 3D printing. The major α-Fe peaks were observed in the samples because the FeCrAl alloy is a solid-solution of Fe with Cr and Al. The DED process is a direct physical deposition of the original material onto the substrate; therefore, the phases of FeCrAl were unchanged during 3D printing.[1]

Fig. 7 shows the microstructural and crystallographic characteristics of the FeCrAl-coated Zr tube sample. SEM images with elemental analyses (Fig. 7(a)) indicate that an FeCrAl layer formed on the Zr substrate. An interfacial mixing zone was observed between FeCrAl and Zr, as well as partial diffusion of Zr into the FeCrAl side. The crystallographic properties were measured using an electron back-scattered diffraction (EBSD) method. The FeCrAl layer possessed elongated grains aligned along the coating's through-thickness direction. The average grain size was approximately 100 μm in length and 20 μm in width. The grains have a random orientation, as shown in Fig. 7(b). The FeCrAl layer matched with single-phase Fe (BCC) (Fig. 7(c)). In the Zr substrate, it was observed to possess a random microstructural orientation with very fine grains. The texture aligned to the (0001) basal pole is typical for Zr material; however, the texture was not developed on the Zr side. The random orientation can be caused by the martensitic phase transformation due to the laser thermal energy [16], which is consistent with our previous report. However, the dark colored band between FeCrAl and Zr is noticeable in Fig. 7(b) and (c). The region appears black because it does not correspond to Fe (BCC) or Zr (HCP). Thus, it is considered that intermetallics and/or amorphous phases are formed at the interface owing to the high thermal energy.

3.2. Oxidation-resistance of FeCrAl-coated Zr-alloy

Fig. 8 shows SEM images of Zr tubes with and without 3D printing FeCrAl layer after the high-temperature oxidation test in steam atmosphere at 1200 °C for 2000 s. As shown in Fig. 8(a), the FeCrAl coating layer on the Zr tube was maintained without delamination or severe oxidation. A thin Al_2O_3 layer (2–3 μm) was formed on the FeCrAl surface due to oxidation. The Al_2O_3 layer was stable and protective; thus, it suppressed further oxidation of the FeCrAl and resulted in an improved resistance to oxidation. Meanwhile, a thick ZrO_2 oxide (~120 μm) was formed on the inner side without coating. In contrast to the stable FeCrAl coating layer, the interface of FeCrAl/Zr was unclear because of the diffusion zone formed by the inter-diffusion of constituent atoms. The diffusion layer is elucidated in Fig. 9. In the case of the fresh Zr tube (Fig. 8(b)), ZrO_2 was formed on the inner and outer sides due to the oxidation of Zr. The thickness of the oxide layer formed on the Zr surface was approximately 120 μm. Below the ZrO_2 layer, a large-grained α-phase and fine-grained prior β-phase of Zr were observed. Because the oxidation test was conducted at temperatures higher than the α → β phase transformation temperature of Zr (863 °C) [17], the prior β-phase is noticeable in the middle of the samples. The prior β-phase is a general term for the phase that underwent the diffusionless phase transformation from the β-phase by cooling. In contrast, α-phase was the phase that did not undergo phase transformation during the oxidation test. The α-phase can be stabilized up to 2130 °C by accommodating O atoms [17]. The grains below the ZrO_2 layer maintained the α-phase by absorbing oxygen diffused from the surroundings. The formation of the oxygen-stabilized α-phase (α-Zr(O)) is typical during high-temperature oxidation of Zr-based alloys [18–20]. According to the microstructure of FeCrAl-coated Zr (Fig. 8(a)), the α-Zr(O) phase was not formed at the interface of the Zr matrix and FeCrAl coating layer. It is suggested that oxygen penetration through the FeCrAl coating layer in the high-temperature oxidation experiment was effectively prevented.

Fig. 9 shows the energy dispersive spectroscopy (EDS) image of the FeCrAl-coated Zr after high-temperature oxidation. A diffusion layer was observed. The depth of FeCrAl diffusion through Zr was approximately 300 μm. The elemental analysis results confirmed the formation of various types of intermetallic compounds, such as $FeZr_2$, $Zr(Fe,Cr)_2$, and $Zr(Fe,Cr)_2$ + Zr, in the Zr substrate. Previously, it was reported that when FeCrAl was coupled with Zr, the inter-diffusion of Zr and Fe and the formation of Zr—Fe intermetallic compounds occurred at high temperatures [21–23]. However, the FeCrAl coating layer remained intact without any delamination or weight loss after the oxidation test. The FeCrAl coating protected the Zr substrate against severe oxidation. It is concluded that the FeCrAl coating using a 3D printing method is highly applicable for the enhanced oxidation resistance of Zr-alloys.

4. Conclusions

In this study, FeCrAl was coated on a Zr tube using a 3D printing DED method to prevent the severe oxidation of Zr at high temperatures. The FeCrAl-coated Zr samples were fabricated based on a parametric study of the processing conditions. The optimal process conditions were 200 W (laser beam power), 10 mm/s (scanning speed), 2.5 g/min (powder supply), and 3 L/min (gas flow). The microstructure of the samples revealed elongated grains of FeCrAl and fine random grains of Zr. The interfacial diffusion zone was observed between FeCrAl and Zr; however, the FeCrAl coating was dense and adhered to the Zr substrate. In a high-temperature oxidation test at 1200 °C for 2000 s, a thin protective Al_2O_3 oxide layer was formed on the surface, which prevented the

[1] These results are provided in supplementary data that are available online.

penetration of oxygen into Zr, leading to an improved oxidation resistance. It is expected that 3D printing technology can be widely utilized to improve the accident-resistance of conventional Zr-alloys.

Supplementary data to this article can be found online at https://doi.org/10.1016/j.surfcoat.2021.126915.

CRediT authorship contribution statement

Il-Hyun Kim: Methodology, Investigation, Writing – original draft. **Yang-Il Jung:** Supervision, Visualization, Writing – review & editing. **Hyun-Gil Kim:** Conceptualization, Project administration. **Jae-Il Jang:** Conceptualization.

Declaration of competing interest

The authors declare that they have no known competing financial interests or personal relationships that could have appeared to influence the work reported in this paper.

Acknowledgments

This work was supported by a National Research Foundation of Korea (NRF) grant funded by the Korean government (MSIT) (No. 2017M2A8A5015058).

References

[1] C. Duriez, T. Dupont, B. Schmet, F. Enoch, Zircaloy-4 and M5 high temperature oxidation and nitriding in air, J. Nucl. Mater. 380 (2008) 30–45.
[2] O. Coindreau, C. Duriez, S. Ederli, Air oxidation of Zircaloy-4 in the 600-1000°C temperature range: modeling for ASTEC code application, J. Nucl. Mater. 405 (2010) 207–215.
[3] J.-H. Park, H.-G. Kim, J.-Y. Park, Y.-I. Jung, D.-J. Park, Y.-C.H. Koo, High temperature steam-oxidation behavior of arc ion plated Cr coating for accident tolerant fuel claddings, Surf, Coat. Technol. 280 (2015) 256–259.
[4] H.-G. Kim, J.-H. Yang, W.-J. Kim, Y.-H. Koo, Development status of accident-tolerant fuel for light water reactors in Korea, Nucl, Eng. Technol. 48 (2016) 1–15.
[5] H.-G. Kim, I.-H. Kim, Y.-I. Jung, D.-J. Park, J.-Y. Park, Y.-H. Koo, Adhesion property and high-temperature oxidation behavior of Cr-coated Zircaloy-4 cladding tube prepared by 3D laser coating, J. Nucl. Mater. 465 (2015) 531–539.
[6] D.J. Park, H.G. Kim, Y.I. Jung, J.H. Park, J.H. Yang, Y.H. Koo, Behavior of an improved Zr fuel cladding with oxidation resistant coating under loss-of-coolant accident conditions, J. Nucl. Mater. 482 (2016) 75–82.
[7] J. Bischoff, C. Delafoy, C. Vauglin, P. Barberis, C. Roubeyrie, et al., AREVA NP's enhanced accident-tolerant fuel developments: focus on Cr-coated M5 cladding, Nucl, Eng. Technol. 50 (2018) 223–228.
[8] T. Dabney, G. Johnson, H. Yeom, B. Maier, J. Walters, K. Sridharan, Experimental evaluation of cold spray FeCrAl alloys coated zirconium-alloy for potential accident tolerant fuel cladding, Nucl. Mater. Eng., 21 (2019) 100715.
[9] K.A. Terrani, S.J. Zinkle, L.L. Snead, Advanced oxidation-resistant iron-based alloys for LWR fuel cladding, J. Nucl. Mater. 448 (2014) 420–435.
[10] C.P. Deck, G.M. Jacobsen, J. Sheeder, O. Gutierrez, J. Zhang, J. Stone, H.E. Khalifa, C.A. Back, Characterization of SiC-SiC composites for accident tolerant fuel cladding, J. Nucl. Mater. 466 (2015) 667–681.
[11] B. Cheng, Y.-J. Kim, P. Chou, Improving accident tolerance of nuclear fuel with coated Mo-alloy cladding, Nucl, Eng. Technol. 48 (2016) 16–25.
[12] B. Marzbanrad, H. Jahed, E. Toyserkani, On the evolution of substrate's residual stress during cold spray process: a parametric study, Mater. Des. 138 (2018) 90–102.
[13] H. Assadi, F. Gartner, T. Stoltenhoff, H. Kreye, Bonding mechanism in cold spraying, Acta Mater. 51 (2003) 4379–4394.
[14] C. Wustefeld, D. Rafaja, M. Motylenko, C. Ullrich, R. Drehmann, T. Grund, T. Lampke, B. Wielage, Local heteroepitaxy as an adhesion mechanism in aluminium coating cold gas sprayed on AlN substrate, Acta Mater. 128 (2017) 418–427.
[15] B. Wang, W. Shi, Z. Miao, Confidence analysis of standard deviational ellipse and its extension into higher dimensional Euclidean space, PLoS One, 10 (2015) e0118537.
[16] Y.-I. Jung, H.-G. Kim, H.-U. Guim, Y.-S. Lim, J.-H. Park, D.-J. Park, J.-H. Yang, Surface treatment to form a dispersed Y2O3 layer on Zircaloy-4 tubes, Appl. Surf. Sci. 429 (2018) 272–277.
[17] T.B. Massalski, Binary Alloy Phase Diagrams, ASM International, Materials Park, 1990, ISBN 0-87170-403-X.
[18] H.-G. Kim, I.-H. Kim, B.-K. Choi, J.-Y. Park, A study of the breakaway oxidation behavior of zirconium cladding materials, J. Nucl. Mater. 418 (2011) 186–197.
[19] M. Reif, F. Scherm, M.C. Galetz, U. Glatzel, An enhanced three-step oxidation process to improve oxide adhesion on zirconium alloys, Oxid, Met. 82 (2014) 99–112.
[20] M. Le Saux, J.-C. Brachet, V. Vandenberghe, A. Ambard, R. Chosson, Breakaway oxidation of zirconium alloys exposed to steam around 1000C, Corro. Sci., 176 (2020) 108936.
[21] D.J. Park, H.G. Kim, J.Y. Park, Y.I. Jung, J.H. Park, Y.H. Koo, FeCrAl and Zr alloys joined using hot isostatic pressing for fusion energy applications, Fusion Eng, Des. 109-111 (2016) 561–564.
[22] X. Han, Y. Wang, S. Peng, H. Zhang, Oxidation behavior ofFeCrAl coated Zry-4 under high temperature steam environment, Corros, Sci. 149 (2019) 45–53.
[23] J. Chen, H. Liu, G. Chi, G. Li, G. Lin, R. Zhang, X. Dai, Effect of rolling on microstructure, shear and tensile strength of diffusion bonded FeCrAl/Zy4 clad plate, Mater. Charact. 169 (2020), 110632.